The Effects of Inlet Guide Vane-Wake Impingement on the Boundary Layer and the Near-Wake of a Rotor Blade

Francesco Soranna
Yi-Chih Chow
Oguz Uzol
Joseph Katz

Department of Mechanical Engineering,
Johns Hopkins University,
Baltimore, MD 21218

This paper examines the response of a rotor blade boundary layer and a rotor near-wake to an impinging wake of an inlet guide vane (IGV) located upstream of the rotor blade. Two-dimensional particle image velocimetry (PIV) measurements are performed in a refractive index matched turbomachinery facility that provides unobstructed view of the entire flow field. Data obtained at several rotor phases enable us to examine the IGV-wake-induced changes to the structure of the boundary layer and how these changes affect the flow and turbulence within the rotor near-wake. We focus on the suction surface boundary layer, near the blade trailing edge, but analyze the evolution of both the pressure and suction sides of the near-wake. During the IGV-wake impingement, the boundary layer becomes significantly thinner, with lower momentum thickness and more stable profile compared with other phases at the same location. Analysis of available terms in the integral momentum equation indicates that the phase-averaged unsteady term is the main contributor to the decrease in momentum thickness within the impinging wake. Thinning of the boundary/shear layer extends into the rotor near-wake, making it narrower and increasing the phase-averaged shear velocity gradients and associated turbulent kinetic energy (TKE) production rate. Consequently, the TKE increases during wake thinning, with as much as 75% phase-dependent variations in its peak magnitude. This paper introduces a new way of looking at the PIV data by defining a wake-oriented coordinate system, which enables to study the structure of turbulence around the trailing edge in great detail. [DOI: 10.1115/1.3149282]

1 Introduction

In multistage turbomachines, the evolution of the rotor boundary layer (BL) is affected by interactions with periodically impinging wakes shed by upstream blade rows. Flow inhomogeneities associated with these wakes inevitably alter the distributions of pressure gradients and turbulence along the blade, and as a result are expected to modify the structure of the BL. A literature review on boundary layer-wake interactions reveals several studies examining the response of boundary layers over stationary walls to, e.g., time-dependent freestream conditions. For example, Patel [1] studied the response of a BL over a splitter plate subjected to a freestream traveling wave, which was generated by periodic oscillations of a wind tunnel exit-nozzle. Dibelius and Ahlers [2] placed an active grid of plates upstream of a flat plate BL. Other types of wake generators have been used to simulate traveling wakes in a turbomachine. For example, Holland and Evans [3] modeled unsteady wake-BL interactions by traversing cylinders in front of a flat plate, whereas Gete and Evans [4] used passing airfoils. Extensive single-point hot wire measurements performed by Halstead et al. [5–8] investigated the effects of boundary layer-wake interactions in multistage axial turbomachines. They concluded that the BL on both compressor and turbine blades changed periodically from laminar to transitional, and to turbulent along paths, which followed the wake trajectory. Mailach and Vogeler observed [9] similar trends and recognized that wake passing was also characterized by an increase in wall shear stress fluctuations. One interesting aspect highlighted by Pfeil and Herbst [10] and Mayle and Dullenkopf [11] was that the wake induced transitional and turbulent strips, which, once generated, propagated at a different speed than that of the generating wake.

The effects of different wake passing frequencies on BL transition were addressed theoretically [11,12], numerically [13,14], and experimentally [15,16]. Liu and Rodi [16] showed that the streamwise location where a flat plate BL became fully turbulent moved upstream with increasing wake-passing frequency. Several experiments conducted in low pressure turbines (e.g., Refs. [17–19]) indicated that wake-induced unsteadiness was also responsible for periodic changes in the size of separation bubbles over the blade suction surfaces. Schobeiri and Öztürk [17] proposed that turbulent fluctuations, introduced by sweeping wakes, energized the separation bubble, causing it to partially disappear. PIV measurements of wake-blade and wake-wake interactions in a multistage turbomachine were also performed by Soranna et al. [20], Chow et al. [21], and Soranna et al. [22]. The present paper continues this effort.

In earlier analysis [23], we showed that the inlet guide vane (IGV) wake impingement indeed causes BL-thinning, but only in the region impinged by the wake. The thinned region traveled with the sweeping wake, and the BL thickened again behind the impingement area. Furthermore, we showed that periodic variations in the pressure field at the edge of the BL were the primary contributors to BL-thinning.

The present paper integrates a relevant brief summary of our previous boundary layer work with new findings, in order to provide a complete description of causes and effects in turbulence production in the rotor near-wake. We examine a region that extends from the blade trailing edge to about $0.1c$, c being the chord length, downstream of it (the terms "upstream" and "downstream" are used while referring to the flow in the relative frame of refer-

Contributed by the International Gas Turbine Institute of ASME for publication in the JOURNAL OF TURBOMACHINERY. Manuscript received November 25, 2008; final manuscript received March 1, 2009; published online May 10, 2010. Review conducted by David Wisler. Paper presented at the ASME Turbo Expo 2008: Land, Sea and Air (GT2008), Berlin, Germany, June 9–13, 2008.

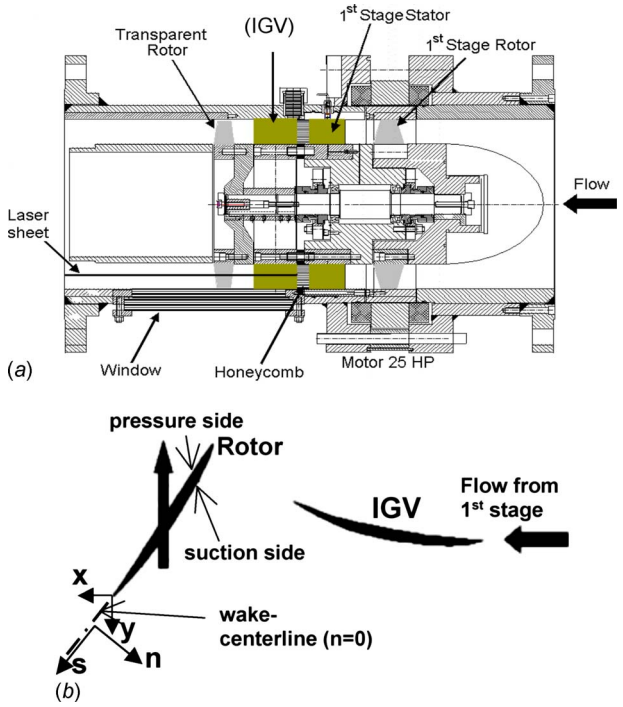

Fig. 1 (*a*) Schematic of the axial turbomachine test section. (*b*) Schematic of IGV blade and rotor blade. Also indicated are the coordinate systems with rotor trailing edge located at $(x/c, y/c)=(1,1)$.

ence). During the IGV-wake passage, turbulent kinetic energy increases in the rotor near-wake region on both the suction and pressure sides. To explain this phenomenon, we examine the phase-dependent variations in production rate of TKE and identify specific contributors to it. The question of how changes in BL scales affect trends of turbulence production is addressed and compared with trends of TKE. Before presenting the results, the facility and experimental setup are described in Sec. 2.

2 Experimental Setup and Procedures

2.1 Facility. The JHU axial turbomachine test facility enables unobstructed PIV measurements within an entire stage of an axial pump, achieved by matching the optical refractive index between the blades and the fluid [24]. The blades are made of a transparent acrylic, whereas the fluid is a concentrated solution of NaI in water (62–64% by weight), with a specific gravity of 1.8 and a kinematic viscosity of 1.1×10^{-6} m^2/s. In the present setup (Fig. 1(*a*)), the two-stage axial turbomachine has four blade rows. A 25 HP, rim-driven motor drives the first stage rotor, which is connected by a common shaft to the second rotor. In the first stage, a rotor is followed by a stator, whereas in the second stage an IGV precedes a rotor row (Fig. 1(*b*)). To minimize the effects of secondary structures generated by the first stage, a honeycomb is installed in the gap between the first-stage stator and the IGV. In the configuration shown in Fig. 1(*a*), the honeycomb occupies this entire gap (it was later shortened [22]). Geometrical parameters of the IGV and rotor blade rows are summarized in Table 1. The design concept of these blades aims at generating desired distribution of swirl downstream of the rotor [25]. All the present measurements are performed under conditions of stable swirl, close to design point, at a rotational speed of 52.3 rad/s. The corresponding Reynolds number based on the rotor blade tip speed and the rotor blade chord is 370,000. Further details can be found in Ref. [21].

Table 1 Geometrical parameters of the second-stage inlet guide vanes and the rotor blade rows

	IGV	Rotor
No. of blades	17	12
Chord c (mm)	50	50
Span h_0 (mm)	44.45	43.25
Aspect ratio	0.89	0.86
Blade thickness (mm)	8.28	7.37 (hub), 5.62 (tip)
Tip clearance (mm)	0	1.2 (2.4% of c)
Pitch to chord ratio	0.97	1.34
Stagger angle[a]	70 deg (tip), 61 deg (midspan), 41 deg (hub)	168 deg
Solidity[b]	0.14	
IGV-rotor gap (mm)	40	
Hub to tip ratio	0.708	

[a]Angle measured from the positive x-axis.
[b]Solidity = span/diameter.

2.2 PIV Setup and Experimental Procedure. Two-dimensional PIV measurements are performed at 50% span, focusing on the rotor BL and its development into the rotor near-wake. The phase-averaged flow and turbulence statistics are investigated in four different rotor phases shifted in time by 1 ms, i.e., 10% of the rotor blade passing period ($T_R=10$ ms). In order to obtain accurate time derivative measurements, experiments were also performed at two additional data sets [23], corresponding to 0.1 ms before and 0.1 ms after phase 2 of the original sets.

A 1-mm-thick light sheet is generated using a neodymium-doped yttrium aluminum garnet (Nd-YAG) laser and images are collected on a 2048×2048 pixel Kodak ES4.0 digital camera. The flow is seeded by 20% silver coated, hollow glass spheres with a mean diameter of 13 μm and a specific gravity of 1.6. Converged turbulence statistics are obtained by recording 500 image pairs at each rotor phase.

Data analysis includes image enhancement, blade signature removal, and cross-correlation analysis using in-house developed software and procedures [26,27,24]. The present 15×15 mm^2 sample area is interrogated with 32×32 pixel windows, using 50% overlapping. Hence, each vector map contains 125×125 vectors, and the vector spacing is 117 μm, i.e., about 0.23% of c. The entire domain of interest is covered by recording and combining data at several neighboring sample areas. A conservative estimate of the uncertainty in mean displacement in each interrogation window is 0.3 pixel, provided the window contains at least five to ten particle pairs [26,27]. For the typical displacement between exposures of 20 pixels, the resulting uncertainty in instantaneous velocity is about 1.5%. Other contributors to uncertainty are addressed in previous publications [24].

From the instantaneous measurements, the phase-averaged velocity components and turbulence statistics are calculated as follows:

$$\bar{U}_i(x,y,\phi)=\frac{1}{N}\sum_{k=1}^{N}(u_i)_k \tag{1}$$

$$\overline{u_i'u_j'}(x,y,\phi)=\frac{1}{N}\sum_{k=1}^{N}[(u_i)_k-\bar{U}_i][(u_j)_k-\bar{U}_j] \tag{2}$$

In the expressions above, $N=500$ is the total number of instantaneous vector maps for each phase, x and y represent the axial and lateral coordinates, respectively, corresponding to subscripts 1 and 2, and ϕ indicates the rotor phase angle. To calculate the turbulent kinetic energy, we directly use its definition: $k(x,y,\phi)=0.5\overline{u_i'u_i'}$.

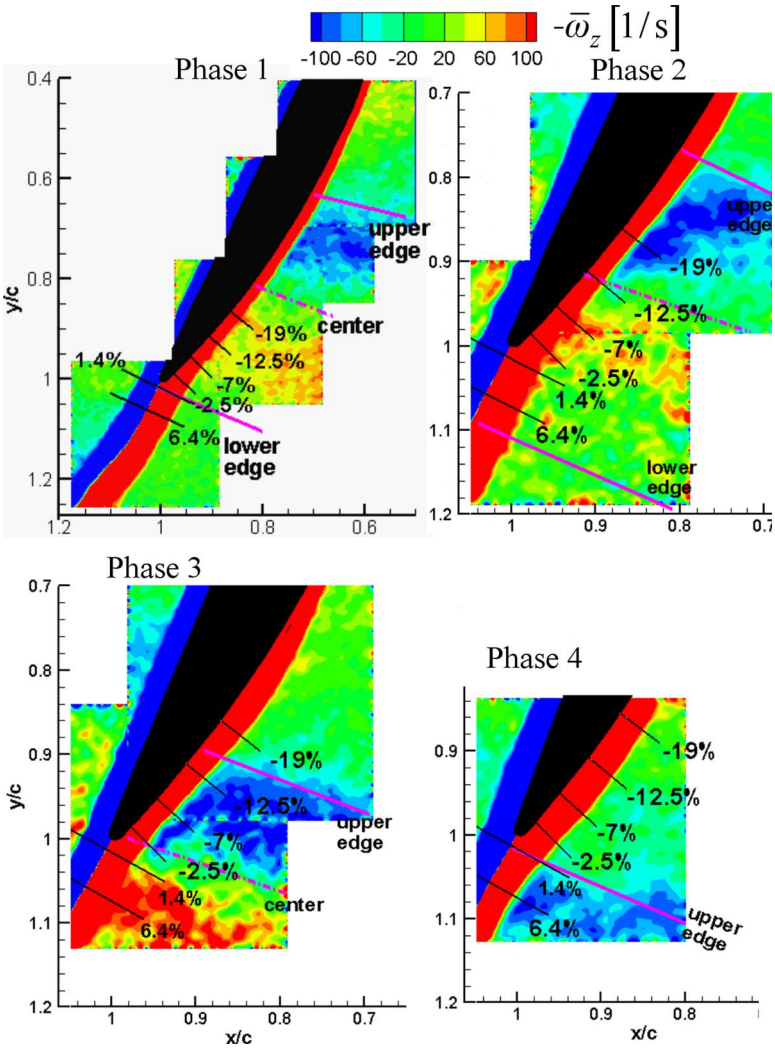

Fig. 2 Distributions of phase-averaged vorticity at four phases. The (x,y) axes are normalized with c. Contour scale is maintained the same at all phases.

However, since we only measure two velocity components (measurements are 2D), we directly measure the contributions of these terms to the kinetic energy and estimate the effect of the missing component by assuming that it is an average of the available components, i.e., $\overline{u_3'u_3'}=0.5(\overline{u_1'u_1'}+\overline{u_2'u_2'})$. Consequently, $k=3/4(\overline{u_1'u_1'}+\overline{u_2'u_2'})$. We calculate k at each phase by ensemble averaging of 500 measurements at the same phase, at every point. Phase-averaged velocity gradients are calculated by second order finite differencing.

We present data in two coordinate systems. As shown in Fig. 1(*b*), the (x,y) coordinate system is fixed in the relative frame of reference. Part of the data analysis is presented in a streamwise (s)-normal (n) coordinate system, which has an origin $(s=0)$ located at the blade trailing edge (TE). Upstream of the latter $(s<0)$, the streamwise axis follows the blade suction surface and velocity components are identified by the superscript b (blade). Downstream of the TE $(s>0)$, s is aligned with the rotor wake centerline defined by the points of minimum phase-averaged vorticity, least squared fitted with a first order polynomial. Thus, orientation of (s,n) varies with phase. The superscript w (wake) identifies velocity components in the rotor wake region. For simplicity, we do not attempt to use body fitted coordinates around the trailing edge, due to large wall curvature there. Variations in flow angle with phase are discussed later.

3 Results

3.1 Location and Characteristics of the IGV Wake. A preliminary step in the analysis of IGV-wake-BL interactions is to identify the approximate boundaries and the center of the impinging IGV wake. To this aim, Fig. 2 presents distributions of $\bar{\omega}_z$, for the same rotor blade but at different four rotor phases. We focus on the trailing edge region. Additional rotor phases analyzing IGV-wake propagation near the leading edge and further downstream of the trailing edge are presented in Refs. [20,21]. To obtain data at a magnification that resolves the outer part of the boundary layer, we have recorded multiple PIV images with partial overlap, each covering 15×15 mm^2. To show the location and impact of IGV-wake impingement on the rotor blade, we have selected and displayed a few of those frames, only those that contain the IGV-wake signature. Consequently, for each phase we show a different number of PIV sample areas, depending on the portion of the rotor blade being impinged by the IGV-wake. In phase 1, we display four adjacent areas, covering more than half of the blade, at a low magnification. In phases 2 and 3, two sample PIV areas are enough to show the region of interest, and in phase 4 only one. As expected, the IGV-wake consists of two distinct $\bar{\omega}_z$ layers of opposite signs. At each rotor phase, the solid lines indicate the upper and lower edges of the IGV wake, estimated based

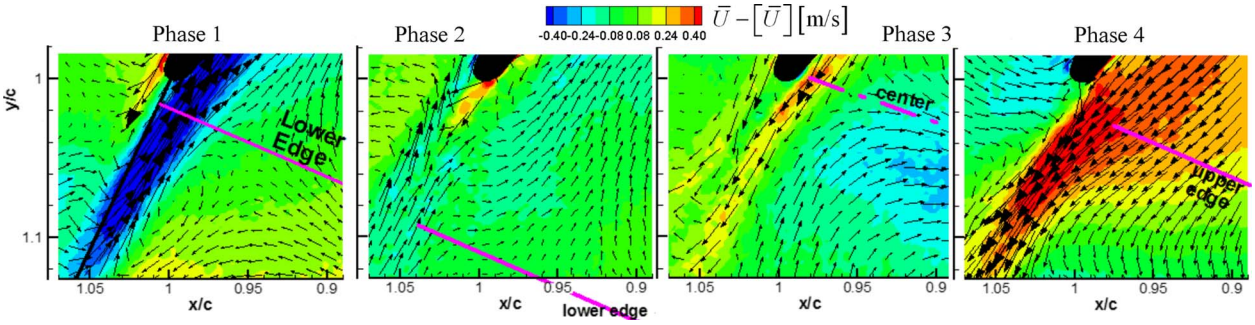

Fig. 3 Contours of axial velocity perturbation at phases 1–4 and perturbation velocity vectors locally scaled with the magnitude of the perturbation velocity

on $\bar{\omega}_z$, and the dashed line marks its center. These lines should provide only qualitative guidance for the location of the IGV wake, except for the points where the IGV-wake intersects with the boundary layer. The IGV-wake segment intersects with the aft part of rotor blade at phase 1 and propagates downwards toward the trailing edge (actually the rotor blade moves upward) in phases 2 and 3. In phase 4, the IGV wake is located downstream of the trailing edge, thus intersecting the rotor wake.

Modifications to the flow field associated with the IGV-wake can be isolated by defining an average velocity as

$$[\bar{U}_i](x,y) = 1/4\sum_{\phi} \bar{U}_i(x,y,\phi) \tag{3}$$

i.e., by taking the average of the phase-averaged velocity field over the available four rotor phases. Then, $\tilde{U}_i = \bar{U}_i(x,y,\phi) - [\bar{U}_i]$ defines wake-induced perturbation of the velocity field. When Eq. (3) is applied to all phases within one rotor blade passage, $[\bar{U}_i]$ defines the average-passage field, and $\tilde{U}_i$ defines the deterministic velocity fluctuation. For the four rotor phases, the overlapping region between the available sample areas extends from $0.02c$ upstream of the TE to about $0.12c$ downstream of it. Figure 3 shows distributions of the axial velocity-perturbation component $\tilde{U}_x(x,y,\phi)$, within the overlap region at all four rotor phases. The velocity-perturbation vectors $(\tilde{U}_x, \tilde{U}_y)$ are also shown. The first effect induced by IGV-wake passage is modification to the velocity field outside of the BL. Let us focus first on trends of phase 3, when the wake centerline intersects the trailing edge. In this case $\tilde{U}_x$ is minimum near the center of the IGV wake, as expected, and the streamlines of the perturbation velocity vector point from the rotor toward the IGVs. Hence, the latter acts as negative jet [28,29], consistent with trends seen in previous studies of, e.g., wake propagation through low pressure turbine cascades [19] and a compressor stage [30]. Before wake impingement, in phase 2, the streamlines of the perturbation velocity point upstream, since the IGV-wake center is located at $s/c \sim -0.125$ (see Fig. 2), above the overlap region. In phase 1 the streamlines split near $s/c = 0.014$, pointing toward different IGV-wake segments upstream and downstream of this region. When the IGV-wake center moves below the overlap region, in phase 4, all the streamlines point downstream, consistent with the location of the IGV-wake center. Here, the values of $\tilde{U}_x$ are particularly high since the orientation of wake-induced velocity is in the same direction as the flow induced by the blade.

The second effect associated with IGV-wake passage is modification of the flow field within the suction and pressure sides BL and near-wake. In phase 1, before wake impingement, the BL on the suction side is characterized by a thick layer of negative $\tilde{U}_x$, which extends to the near-wake region. The BL is clearly thicker than in subsequent phases and develops into a relatively thick shear layer in the region just downstream of the trailing edge. In phase 2, but especially in phase 3, as the IGV wake enters the overlap region, the flow within the BL and the near-wake accelerates, and the boundary/shear layer becomes substantially thinner compared with phase 1. These trends are consistent with the positive values of $\tilde{U}_x$. In the last phase, as the IGV-wake-induced flow is aligned with the rotor blade orientation (unlike phases 2 and 3), the flow within the boundary/shear layer is further accelerated. As will be shown in Secs. 3.2–3.6, these phase-dependent changes in the structure of the flow near the trailing edge have a profound impact on the distribution of velocity gradients in this region and, ultimately, on the production rate of TKE.

We have also calculated and examined the distribution of perturbation vorticity, $\tilde{\omega}_z = \bar{\omega}_z(x,y,\phi) - [\bar{\omega}_z]$. Consistent with Wheeler et al. [30], and with Fig. 2, the distribution of $\tilde{\omega}_z$ outside of the BL but within the IGV wake (not shown) is characterized by a two layer structure, with a $\tilde{\omega}_z < 0$ layer preceding a $\tilde{\omega}_z > 0$ layer. This distribution points at the same locations of the edges and center of the IGV-wake as those identified by vorticity distribution (Fig. 2) and axial velocity perturbation (Fig. 3). Unlike in the results of Wheeler et al. [30], the two layer structure is overwhelmed within the boundary layer by high $\bar{\omega}_z$ levels resulting from phase-dependent variations to the BL structure.

3.2 Modifications to the Velocity Gradients in the Near-Wake. To understand turbulence production trends, it is important to analyze first the effects of IGV-wake impingement on the phase-averaged velocity gradients in the near-wake. The analysis is performed in the streamwise-normal coordinate system but data are presented on the (x,y) mesh. To avoid body fitting of the trailing edge, for the purpose of analyzing the near-wake, the s-axis defined by the wake centerline is also employed in the region upstream of the TE.

Figure 4 shows the distributions of $\bar{U}_s^w$ and $\partial \bar{U}_s^w / \partial n$ at phases 1–4. The edges of the impinging IGV wake are marked by solid lines labeled as 'Upper Edge' or 'Lower Edge' when these edges are located within the field of view. The center of the IGV wake is identified by the dashed-dotted line labeled as 'Center.' The white line shown in each plot identifies the rotor wake centerline, as defined by least squares fitting the $\bar{\omega}_z = 0$ points along the rotor wake. The latter is characterized by a low streamwise velocity region (in the relative reference frame), which is dissected by the $\bar{\omega}_z = 0$ line. As discussed and explained in Secs. 3.3 and 3.4, during IGV-wake passage near the trailing edge of the suction side, the BL-thickness decreases. Consequently, the widths of the rotor near-wake, i.e., the region with very low $\bar{U}_s^w$, also decrease. Phase 1 represents conditions prior to wake passage, when the IGV-wake center is located well upstream of the trailing edge, whereas phase 3 shows the near-wake during IGV-wake impingement on the trailing edge. These scale changes and their effects are clearly evident on the suction side of the rotor near-wake, but not on the pressure side, as discussed in more detail in Sec. 3.3. The values

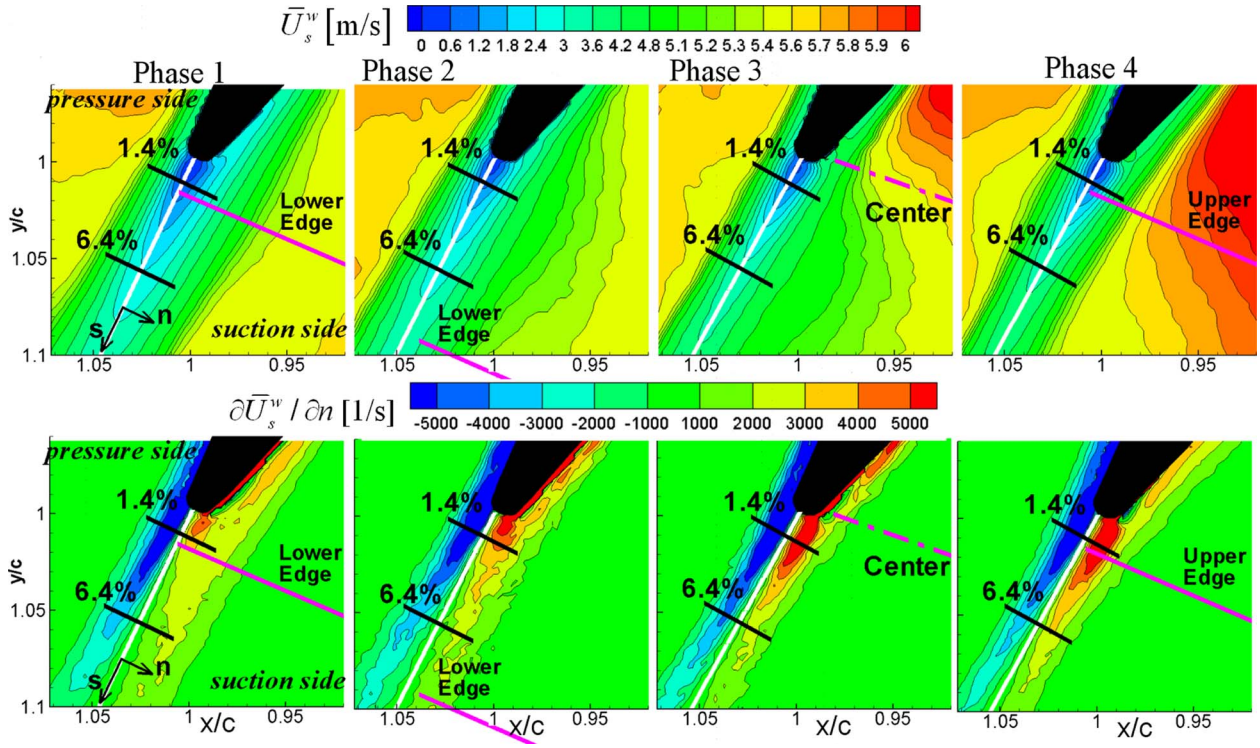

Fig. 4 First row: distributions of $\bar{U}_s^w$ in the (s,n) coordinate system defined by the rotor wake centerline (white lines) at phases 1–4. Second row: distribution of cross stream gradient of $\bar{U}_s^w$.

of $\partial\bar{U}_s^w/\partial n$ on the suction side increase from phase 1 to phase 4, while the peaks move closer to the rotor wake centerline. The levels of $\partial\bar{U}_s^w/\partial n$ are consistently higher on the pressure side but are less susceptible to phase variations. To the right of the trailing edge, at $y/c \sim 1$, in phases 1, 3, and 4, there is a narrow region of low $\partial\bar{U}_s^w/\partial n$ along the suction side wall. The streamlines of the phase-averaged velocity, shown in Fig. 5 for phase 4, indicate that local flow separation occurs in this region. Indeed $\bar{U}_n$ is positive and $\bar{U}_s$ has a local peak here (Fig. 5), causing a reduction in $\partial\bar{U}_s^w/\partial n$ and an inflection in the $\bar{U}_s^w$ profile (not shown). Consequences of this phenomenon on turbulence production will be addressed later.

Of the velocity gradients, which are not shown here, $\partial\bar{U}_s^w/\partial s$ is characterized by positive peak values along the wake centerline,

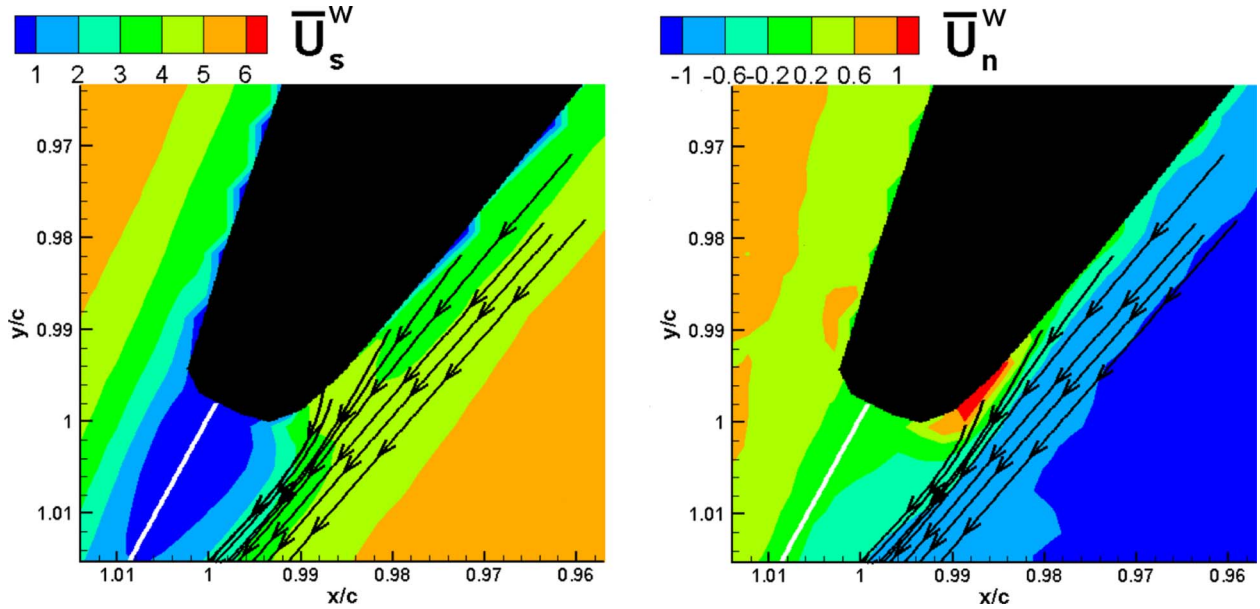

Fig. 5 Distributions of $\bar{U}_s^w$ and $\bar{U}_n^w$ at phase 4 near the rotor trailing edge. The arrowed lines indicate streamlines of the phase-averaged velocity vector.

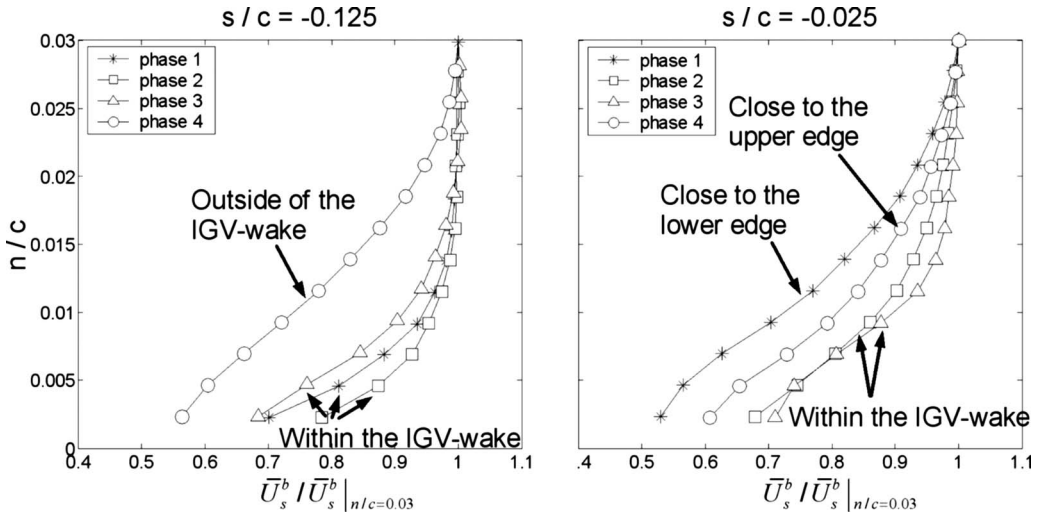

Fig. 6 Profiles of $\bar{U}_s^b$ at $s/c=-0.125,-0.025$

as expected. The $\partial \bar{U}_n^w / \partial n$ gradients show similar trends to those of $\partial \bar{U}_s^w / \partial s$, but with opposite sign. Their magnitudes are comparable in the near-wake (continuity at midspan), but in regions of flow separation $|\partial \bar{U}_n^w / \partial n| > |\partial \bar{U}_s^w / \partial s|$. Finally, $\partial \bar{U}_n^w / \partial s$ is small compared with $\partial \bar{U}_s^w / \partial n$.

Before concluding, it is worthwhile to mention that just downstream of the trailing edge, large changes in flow angle (α) occur along the wake centerline. For example, at $s/c=0.014$, $\alpha=36$ deg before wake impingement (phase 1) and increases by as much as 66%, to 60 deg, during wake impingement (phase 3).

3.3 Phase-Averaged Velocity Profiles. To analyze phase-dependent changes in velocity within the boundary layer and in the near-wake, we extract sample profiles of the phase-averaged streamwise velocity component, in the relative frame of reference. Results for the suction side boundary layer are presented in Fig. 6 and for the rotor near-wake in Figs. 7 and 8. The first two stations, ($s/c=-0.125$ and $s/c=-0.025$) are located within the suction side boundary layer (see locations Fig. 2). Here, the location of the $n/c=0$ point coincides with the intersection of the local n-plane with the blade suction surface. The near-wake stations ($s/c=0.014$ and $s/c=0.064$) are located across the rotor near-wake, with $n/c=0$ at the wake centerline. In this section, during boundary layer analysis, $\bar{U}_s^b$ is the velocity parallel to the blade surface, while $\bar{U}_s^w$, as before, is the velocity component parallel to the rotor wake centerline.

To highlight trends within the boundary layer, the profiles are normalized with local streamwise velocity measured at the maxi-

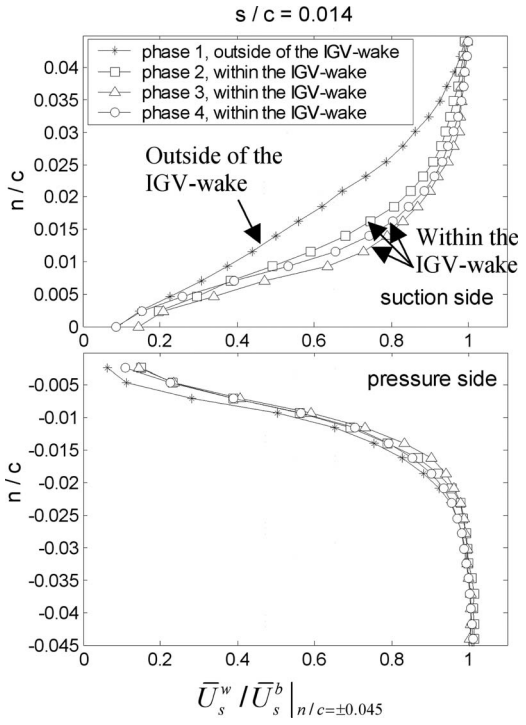

Fig. 7 Profiles of $\bar{U}_s^w$ at $s/c=0.014$ indicated in Fig. 2

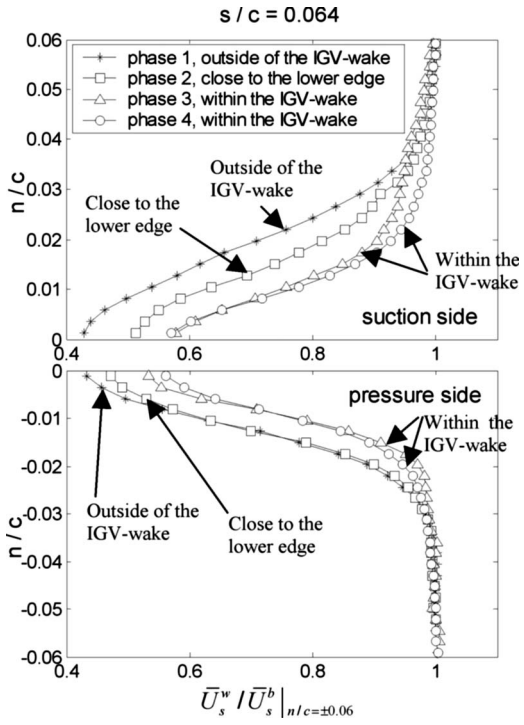

Fig. 8 Profiles of $\bar{U}_s^w$ at $s/c=0.064$ indicated in Fig. 2

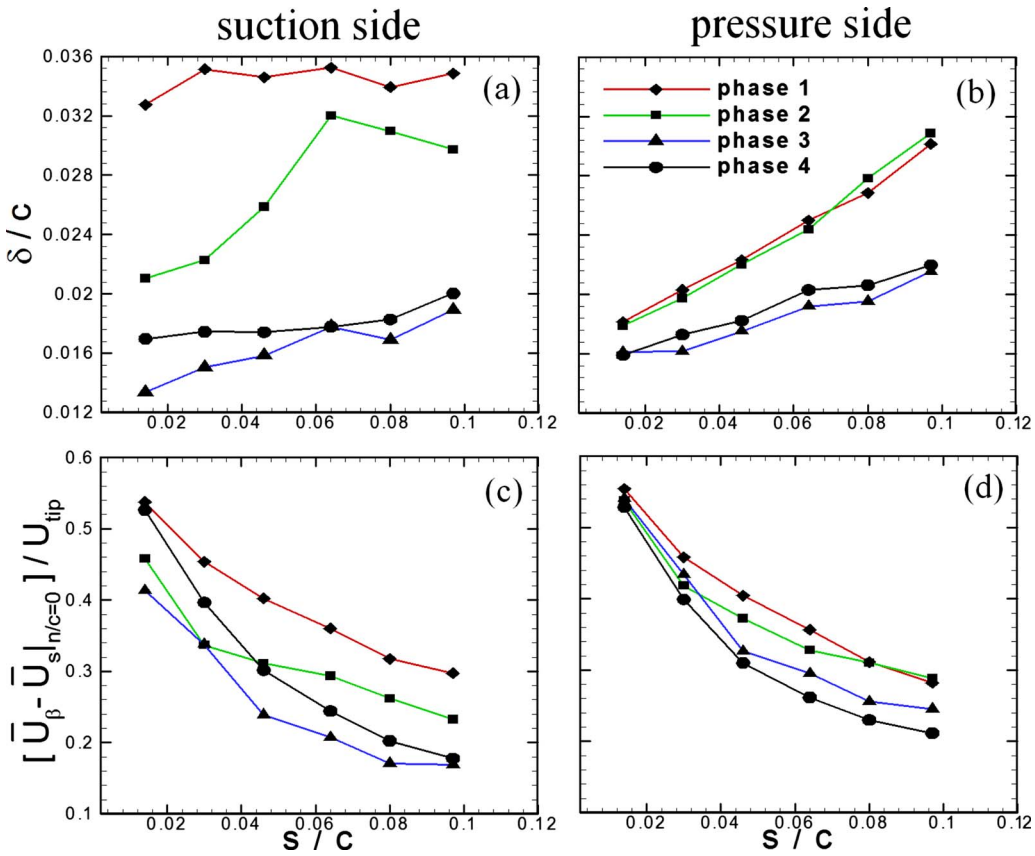

Fig. 9 Streamwise variation of ((*a*) and (*b*)) wake length scale δ_β and ((*c*) and (*d*)) wake deficit $[\bar{U}_\beta(s)-\bar{U}_s(s,0)]$ along the suction and pressure sides at four rotor phases

mum n/c value shown for each profile. For example at $s/c=-0.125$, profiles are normalized with respect to $\bar{U}_s^b|_{n/c=0.03}$. When this station is located outside of the IGV-wake, as in phase 4, the boundary layer is clearly thicker than other phases, and the $\bar{U}_s^b$ profile develops an inflection point (Fig. 6). At phases 1–3, the same station is located within the impinging IGV wake and the BL is thinner. Furthermore, disappearance of the inflection point indicates that the BL is less likely to separate compared with conditions outside of the wake. At $s/c=-0.025$, all the profiles, except for the one corresponding to phase 2, show inflection points, indicating that elevated adverse pressure gradients strongly affect the boundary layer stability at all phases. Recall that in this region, the streamlines tend to separate. Nevertheless, the boundary layer impinged by the wake, i.e., in phases 2 and 3, is thinner compared with profiles at the edge of the wake. Specific causes for this phenomenon are discussed in Sec. 3.4.

Before describing phase-dependent changes to rotor wake profiles, we introduce suitable estimates of length and velocity scales of the near-wake. As described in Ref. [21], for a wake exposed to a nonuniform flow, one cannot uniquely define the wake-width and the velocity deficit based on the external velocity. Instead, at each streamwise plane, we identify the wake length scale, δ_β, as the distance from the center of the wake to a point where $\partial\bar{U}_s/\partial n$ is one-half of the average shear strain rate, i.e.,

$$\partial\bar{U}_s/\partial n|_{n=\delta_\beta}=0.5(\bar{U}_s|_{n=\delta_\beta}-\bar{U}_s|_{n=0})/\delta_\beta \tag{4}$$

In place of using the external velocity to define a deficit, we use $\bar{U}_\beta$, i.e., the velocity at a distance δ_β from the rotor wake-center. Due to the asymmetry of the rotor wake, each side of the wake has its own length and velocity scales, and is calculated separately. Distributions of δ_β and $[\bar{U}_\beta(s)-\bar{U}_s(s,0)]$, i.e., the "velocity deficit," are presented in Fig. 9. Additional information on variations of wake scales is presented in Refs. [21,22] for the same wake, but at different phases and greater distances from the trailing edge.

Downstream of the rotor trailing edge, at $s/c=0.014$ (Fig. 7), the wake thickness decreases at phases 2–4, when this station is located within the IGV-wake. On the suction side, $\delta_\beta\sim0.032c$ at phase 1 and decreases by as much as 60% at phase 3. The reduction in the velocity deficit between these phases is 22%. These trends persist over the entire near-wake (Fig. 9). On the pressure side, the largest changes to wake scales occur between phases 1 and 4, but they are smaller than those on the suction side.

Similar trends persist further downstream, at $s/c=0.064$ (Figs. 8 and 9), i.e., as the IGV wake arrives, the rotor wake thickness progressively decreases, and the flow within the rotor wake accelerates. Notice that on the pressure side the profiles collapse onto two different sets, depending on weather this station is located within the IGV-wake or outside of it.

3.4 Contributors to the Evolution of Boundary Layer Thickness. As previously shown, the process of thinning of the rotor wake has its origin in the changes that occur in the BL. The question is what is the underlying mechanism leading to reduction in BL-thickness in regions impinged by the IGV wake. In this section, we address this question, following boundary layer (only) analysis already presented in previous conference papers [23].

We have selected one of the phases, phase 2, and recorded data for an additional phase, denoted as 2′, in order to achieve a higher time-resolution (of 0.1 ms) that is similar to the dimensionless spatial resolutions, which is essential for analyzing the evolution of momentum thickness in the boundary layer. We focus on the BL-suction side, where phase-dependent variations in scales are more pronounced. In this additional data set, the IGV-wake center is located very close to the trailing edge, and its location is also

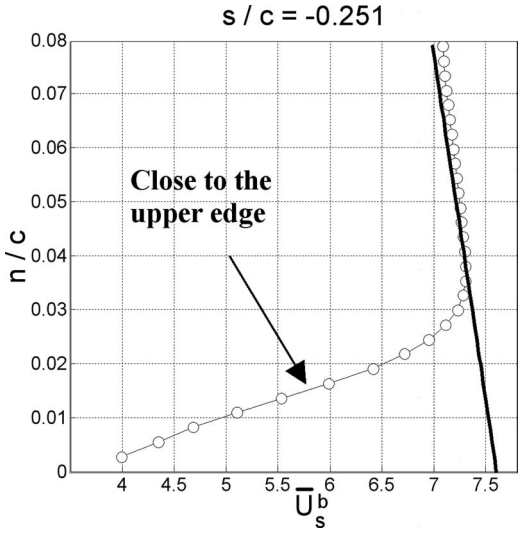

Fig. 10 Phase-averaged boundary layer profile at phase 2′. The solid line represents the distribution of the potential velocity $\bar{U}^b_{ps}$.

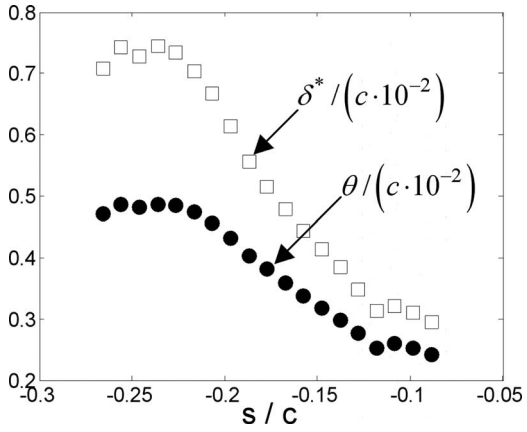

Fig. 11 Distribution of δ^*, and θ at phase 2′

identified from vorticity distributions (not shown here). Distributions of phase-averaged velocity, vorticity, turbulent kinetic energy, and Reynolds stresses can be found in Ref. [23]. A sample boundary layer profile at a location close to the upper edge of the impinging wake is shown in Fig. 10. Downstream of this location, boundary layer thinning and penetration of high momentum flow closer to the wall accelerate the flow in the streamwise direction.

To quantify effects of BL-thinning, we calculate values of displacement and momentum thicknesses given by [31]

$$\delta^* \equiv \int_0^\infty \left(1 - \frac{\bar{U}^b_s}{\bar{U}^b_{ps}}\right) dn, \quad \theta \equiv \int_0^\infty \frac{\bar{U}^b_s}{\bar{U}^b_{ps}}\left(1 - \frac{\bar{U}^b_s}{\bar{U}^b_{ps}}\right) dn \tag{5}$$

where $\bar{U}^b_{ps}$ is the potential velocity, assumed to be prevalent outside of the boundary layer. It is obtained from a condition of irrotationality outside of the boundary layer, i.e., by setting

$$\bar{\omega}_z = -\partial \bar{U}^b_{ps}/\partial n - \kappa \bar{U}^b_{ps} = 0 \tag{6}$$

where $\kappa = 1/R$ is the suction surface curvature. Solving for $\bar{U}^b_{ps}$, this equation yields

$$\bar{U}^b_{ps} \simeq U_{pw} e^{-\kappa n} \approx U_{pw}[(1 - \kappa n) + O(kn)^2] \quad \text{as} \quad n \to 0 \tag{7}$$

where U_{pw} is the potential velocity at the blade surface, i.e., the velocity that would exist there in the absence of a boundary layer. The distribution of $\bar{U}^b_{ps}$, estimated from Eq. (7), is included in Fig. 10, and indeed matches the linear trends of velocity profiles outside of the boundary layer.

Distributions of δ^* and θ within the wake impingement region ($s/c > -0.25$) for phase 2′ are presented in Fig. 11. Clearly, both boundary layer length scales decrease within the impinging wake, a trend unexpected in a diffusion-dominated region. Wheeler et al. [30] recently reported similar trends in a compressor blade where boundary layer thickening lags behind regions of wake impingement.

To examine how IGV-wake impingement causes reduction in BL-scales, we calculate available terms in the evolution equation of the momentum thickness, given by

$$\frac{d\theta}{ds} = -\frac{1}{U^2_{pw}} \frac{\partial}{\partial t} \int_0^\infty (\bar{U}^b_{ps} - \bar{U}^b_s) dn - (H+2) \frac{\theta}{U_{pw}} \frac{dU_{pw}}{ds} + \frac{u^2_\tau}{U^2_{pw}} + q \frac{d\kappa}{ds} - \frac{2}{U^2_{pw}} \int_0^\infty \Omega_n \bar{U}_r dn \tag{8}$$

where

$$q = \int_0^\infty n\left(1 - \frac{\bar{U}^b_s}{\bar{U}^b_{ps}}\right) dn + 2\int_0^\infty n \frac{\bar{U}^b_s}{\bar{U}^b_{ps}}\left(1 - \frac{\bar{U}^b_s}{\bar{U}^b_{ps}}\right) dn \tag{9}$$

Equation (8) was derived from the steady, two-dimensional momentum equations in curvilinear coordinates given by So and Mellor [31], and adding unsteady and Coriolis terms [23]. In this equation, Ω_n is the n-component of the angular velocity vector of the turbomachine, and $\bar{U}_r$ is the radial phase-averaged velocity. The first two terms on the right hand side represent, in order, the impact on $d\theta/ds$ of the unsteady and convective acceleration at the edge of the BL, which inherently dominate the local pressure gradients. The last three terms are the wall shear stress term, the contribution due to surface curvature, and the contribution of the Coriolis force, respectively. The latter must be considered when analysis is performed in a rotating (i.e., noninertial) frame of reference. Since in the present case the relative velocity vector is obtained by subtracting a constant blade speed at every point, the reference frame is inertial and the Coriolis force should not be included. Nevertheless, its magnitude, roughly estimated from stereo PIV data that has a lower spatial resolution [22] is only about, e.g., 12% of the unsteady term at $s/c = -0.18$.

The available terms in the integral momentum equation are presented in Fig. 12. The values of $d\theta/ds$ have the highest negative magnitude between $s/c = -0.2$ and $s/c = -0.12$, i.e., within the impinging IGV-wake. It is also evident that trends of the unsteady term (first term, right hand side of Eq. (8)) are consistent with those of $d\theta/ds$, whereas the convective (second) term of Eq. (8), being positive and substantial, clearly cannot cause a reduction in θ. Of the remaining terms, the one containing $d\kappa/ds$, i.e., the streamwise variations in curvature, is negligible for the present geometry. The wall shear stress term is always positive, i.e., it cannot reduce the boundary layer thickness. Its magnitude (not shown), estimated using the maximum Reynolds shear stress value within the boundary layer, is at least two order of magnitude smaller than the unsteady term.

Thus, of the terms presented here, the unsteady term seems to be the only contributor to boundary layer thinning within the impinging IGV wake. Note, however, that combining all the available terms on the right hand side of Eq. (8) results in values that are higher than $d\theta/ds$, i.e., the two-dimensional integral momen-

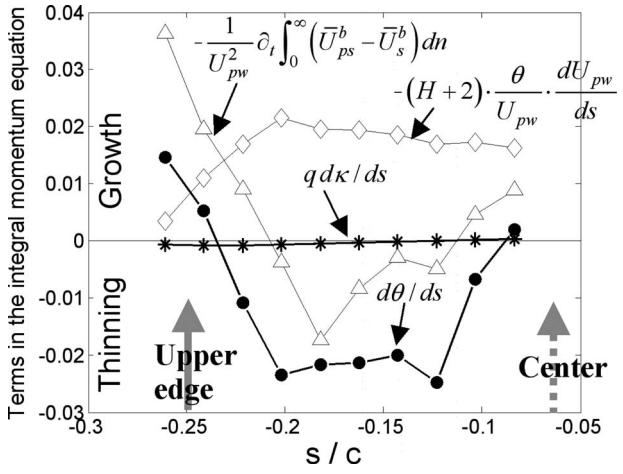

Fig. 12 Available terms in the evolution equation of momentum thickness (8)

tum equation is not satisfied. Thus, contribution of out-of-plane terms, which are not available from the planar PIV data, must be also included in order to balance the integral momentum equation. A brief discussion on missing terms is provided in Ref. [23]. Yet, the agreement between trends of $d\theta/ds$ and the unsteady term suggests that they are closely related. Thus, variations in this term imply that boundary layer thinning is caused by phase-dependent changes to the pressure distribution, i.e., to blade loading.

3.5 Turbulence Distribution Around the Trailing Edge. In this section, we analyze the phase-dependent evolution of Reynolds stresses and turbulent kinetic energy in the near-wake. Figure 13 shows distributions of the available Reynolds stress tensor components, calculated in the (s,n) coordinate system defined by the wake centerline, and plotted in the (x,y) grid. To highlight the level of anisotropy between normal Reynolds stresses, we intentionally maintain the same contour scales in their corresponding contour plots (but not in the contour plots of shear stress). Indeed, in the near-wake, $\overline{u_s'^2}$ is much larger than $\overline{u_n'^2}$, i.e., $\overline{u_s'^2}$ is the dominant stress term contributing to k. This trend is consistent with previous measurements of streamwise and normal turbulent intensities in the wake of, e.g., airfoil at incidence [32]. Notice that magnitudes of $\overline{u_n'^2}$ and $\overline{u_s'^2}$ are comparable only to the right of the trailing edge at phases 1, 3, and 4. In this region, flow separation causes misalignment between the s coordinate and the local streamline orientation (Fig. 5), resulting in redistributions of the velocity fluctuations between the s and n directions and change of sign in $\overline{u_s'u_n'}$. Furthermore, in Sec. 3.6 we show that associated compression in the normal direction, i.e., $\partial\bar{U}_n^b/\partial n<0$, contributes substantially to turbulence production in this region. In phases 1 and 2, distinct layers of high streamwise fluctuations develop along the suction and pressure sides of the near-wake. The suction side layer is relatively thick and characterized by nonmonotonic decay with streamwise distance. On the pressure side, peaks of $\overline{u_s'^2}$ occur in close proximity of the trailing edge. These trends change substantially at phases 3 and 4. As the rotor wake becomes thinner, there is a substantial increase in streamwise fluctuations around the trailing edge, followed by monotonic decay downstream of it. Wake thinning also brings peaks of $\overline{u_s'^2}$ closer to the rotor wake centerline, especially on the suction side. Distributions of TKE whose trends and nonuniformities are inherently very similar to those of $\overline{u_s'^2}$ are also presented in Fig. 13. Clearly, as the IGV wake sweeps past the trailing edge, the TKE-levels become increasingly higher in the pressure and suction side boundary layer and in the near-wake region, peaking in phase 4. Further details on TKE-trends are discussed and compared with those of TKE production rate in the next section.

The values of $\overline{u_n'^2}$ generally peak close to the rotor wake centerline. Thinning of the rotor wake, as a result of IGV-wake passage, reduces $\overline{u_n'^2}$ in the outer regions. The shear stress, $\overline{u_s'u_n'}$, changes sign across the rotor wake centerline, as expected, with negative values located on the suction side of the wake. As the width of the wake decreases, the largest (in magnitude) values of $\overline{u_s'u_n'}$ move upstream, toward the trailing edge.

3.6 Effects of Production Rate on the Distribution of Turbulent Kinetic Energy. A useful method for understanding the phase-dependent evolution of turbulence around the trailing edge involves studying the effects of the source term in the transport equation for TKE [33]:

$$\frac{\bar{D}k}{\bar{D}t}+\Pi=P-\tilde{\varepsilon}+\nu\nabla^2k \tag{10}$$

In this equation, $P=-\overline{u_i'u_j'}\,\partial\bar{U}_i/\partial x_j$, the production rate of TKE, is the only term that generates new turbulence. Of the other terms, Π is a transport term involving turbulence and pressure, i.e., it does not produce new turbulence, and $\tilde{\varepsilon}$ is the pseudodissipation. In general, one should expect to observe an increase in k in regions of high P and a decrease in TKE when P is small or even negative. It would be useful to calculate P and compare it to trends of turbulent kinetic energy. For a two-dimensional streamwise-normal coordinate system,

$$P=-\overline{u_s'^2}\frac{\partial\bar{U}_s}{\partial s}-\overline{u_n'^2}\frac{\partial\bar{U}_n}{\partial n}-\overline{u_s'u_n'}\frac{\partial\bar{U}_s}{\partial n}-\overline{u_s'u_n'}\frac{\partial\bar{U}_n}{\partial s} \tag{11}$$

This equation does not include out-of-plane terms that cannot be calculated from 2D data. However, as shown in Ref. [22] using (lower resolution) stereoscopic PIV data obtained in multiple, closely spaced planes, these terms are small in the near-wake region.

Figure 14 shows distributions of production rate along with dominant terms contributing to it. At phase 1, i.e., prior to IGV-wake impingement, production is high over the entire rotor near-wake, consistent with trends of k. On the suction side, high values of k and P extend to large n/c. The shear production term dominates everywhere, consistent with distributions of $-\overline{u_s'u_n'}$ and $\partial\bar{U}_s^w/\partial n$, overcoming mostly negative values of $-\overline{u_s'^2}\,\partial\bar{U}_s^w/\partial s$. Thinning of boundary/shear layer due to IGV-wake impingement in phase 2 increases $\partial\bar{U}_s^w/\partial n$, further enhancing the shear production term, but along a narrower region. In phase 3, the wake is very thin, but the rapid decay of shear stress along the suction side confines the high production region to the very near-wake. The effects of IGV-wake-induced thinning starts reversing during phase 4, as the boundary layer upstream of the trailing edge starts widening when the IGV wake clears the trailing edge (see velocity profiles in Fig. 6). This trend is particularly evident in the distributions of $-\overline{u_s'u_n'}\,\partial\bar{U}_s^w/\partial n$.

For most of the near-wake, $-\overline{u_s'^2}\,\partial\bar{U}_s^w/\partial s$ is negative due to an increase in streamwise velocity along the wake. The only exception is the region surrounding the trailing edge, in part due to the selected coordinate system, and in part due to flow separation, as discussed before. The values of $-\overline{u_n'^2}\,\partial\bar{U}_n^w/\partial n$ are significantly smaller than other terms except for the trailing edge region along the suction side, and in the center of the wake at phase 4. Notice that this term appears as a source in the evolution equations for both k and $\overline{u_n'^2}$ (the latter is not shown, see Ref. [33]), consistent with the elevated $\overline{u_n'^2}$ along the suction side boundary layer. This term is a result of high $-\partial\bar{U}_n^w/\partial n$ as the boundary layer starts separating near the trailing edge (Fig. 5).

Figure 15 compares profiles of P and k in the near-wake in two streamwise planes. Agreements for the most part are clearly evi-

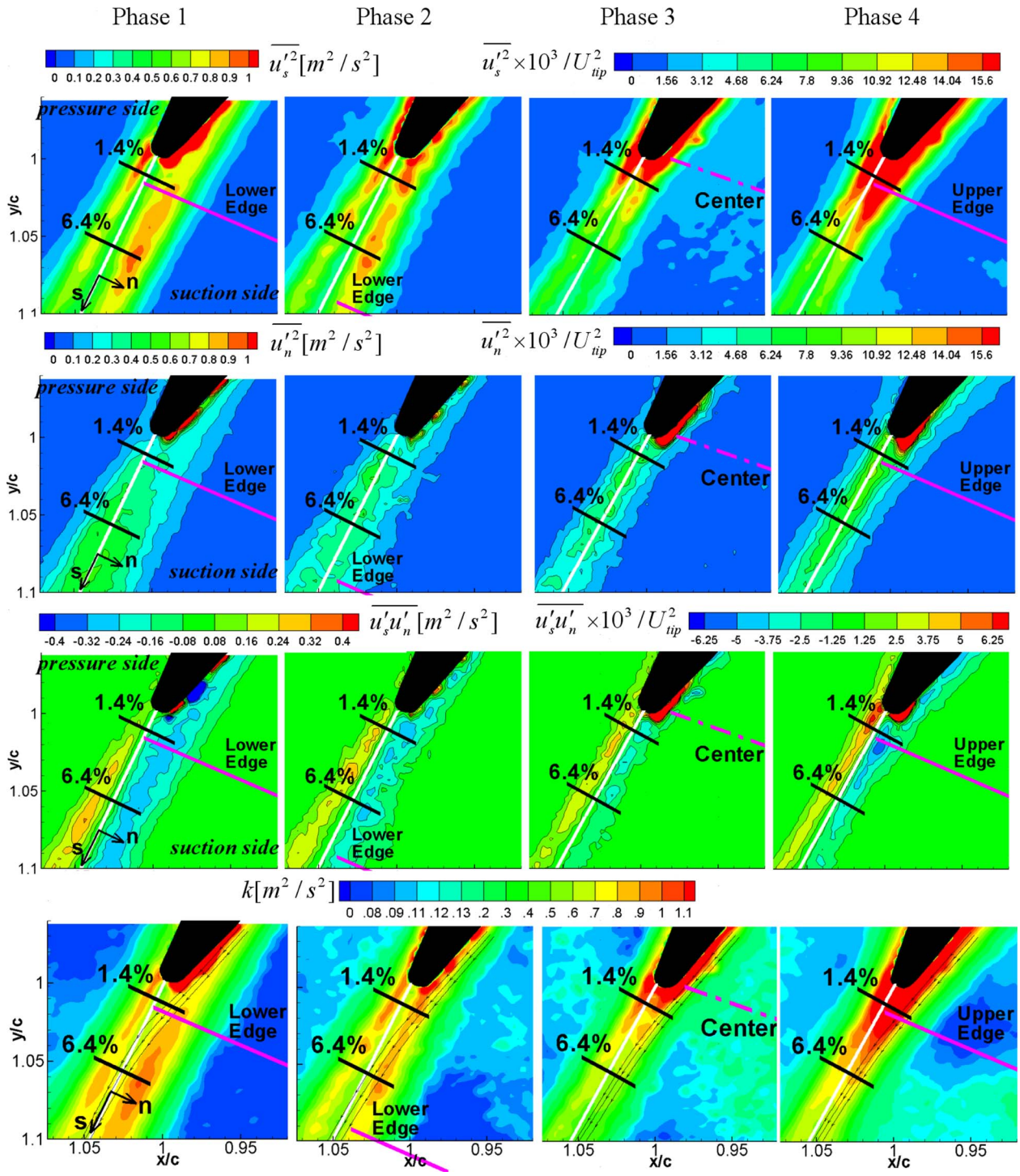

Fig. 13 First three rows: distributions of $\overline{u_s'^2}$, $\overline{u_n'^2}$, and $\overline{u_s'u_n'}$ at four rotor phases. Last row: distribution of TKE.

dent. At $s/c=0.014$ (Figs. 15(*a*) and 15(*b*)) and along the suction side, both profiles show effect of boundary layer and near-wake thinning between phases 1 and 3, as well as the reversal, i.e., beginning of wake broadening in phase 4. There are small variations in peak magnitudes of either P or k at phases 1–3, but both are clearly larger during phase 4, where k increases by as much as ~75%. On the pressure side, there are little phase-dependent variations in width of profiles, but again, both P and k peak at phase 4. At $s/c=0.064$ (Figs. 15(*c*) and 15(*d*)), trends of thinning between phases 1–3 and reversal in phase 4 persist. However, here the lowest P and k occur during phase 3, a trend associated with fast decay of the shear stress in the near-wake, and corresponding reduction in production rate.

We cannot explain, at least based on the present data, why differences in production rate between the pressure and suction sides of the near-wake sometimes do not cause similar differences in distributions of TKE. For example, at phase 4 and $s/c=0.014$, the suction side production is significantly lower than that in the pressure side, yet values of TKE are not significantly different. The same applies to phases 1, 3, and 4 at $s/c=0.064$. To explain

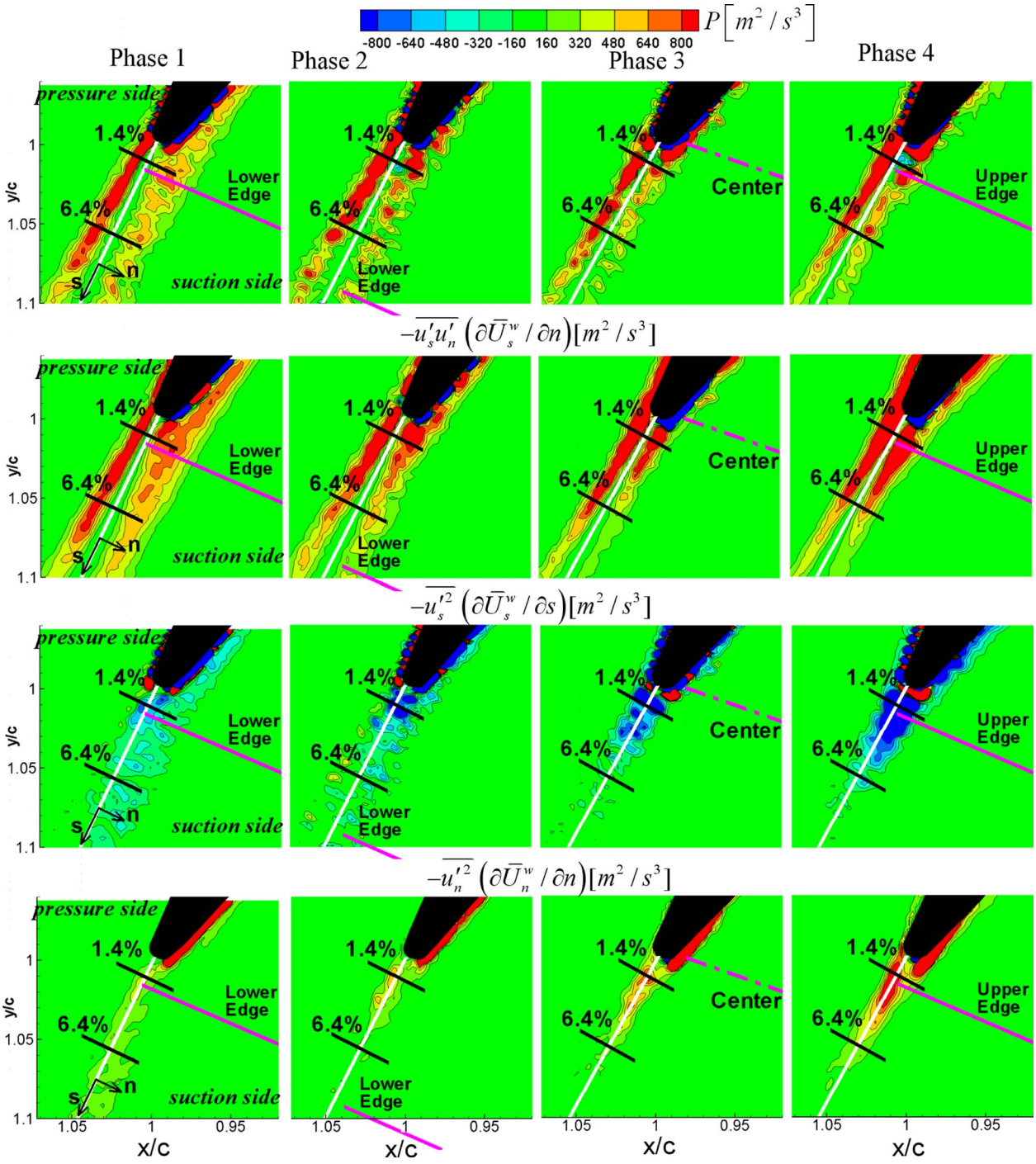

Fig. 14 Top to bottom rows, distributions of production rate of TKE (first row) and the terms contributing to it (Eq. (11)): $-\overline{u_s'u_n'}\partial\bar{U}_s^w/\partial n$ (second row), $-\overline{u_s'^2}\partial\bar{U}_s^w/\partial s$, and $-\overline{u_n'^2}\partial\bar{U}_n^w/\partial s$ (third and fourth rows). Data are presented in the (s,n) coordinate system defined by the wake centerline and plotted in the (x,y) grid.

these discrepancies, one has to follow the time evolution of TKE, accounting also for mean advection and transport term. For example, TKE production in the boundary layers upstream of the rotor wake may be (most likely) different, feeding different turbulence into the near-wake. Unfortunately, the resolution of the present measurements is not sufficient for determining the TKE and its production rate in peak regions in the inner parts of the boundary layer. Future studies will address this issue. Trends of the advection terms (not shown) are also different. For example, at phase 4, advection by the phase-averaged flow on the suction side is of the same sign as the production term, both increasing, whereas on the pressure side the advection term is negative. When combined, the differences between suction and pressure sides diminish.

4 Conclusions

Impingement of an IGV wake on a downstream rotor blade alters the structure of the boundary layer, especially on the suction side, by changing periodically its scales and profiles. Reduction in boundary layer thickness is observed in regions impinged by the wake, along with more stable profiles, whereas BL-growth occurs

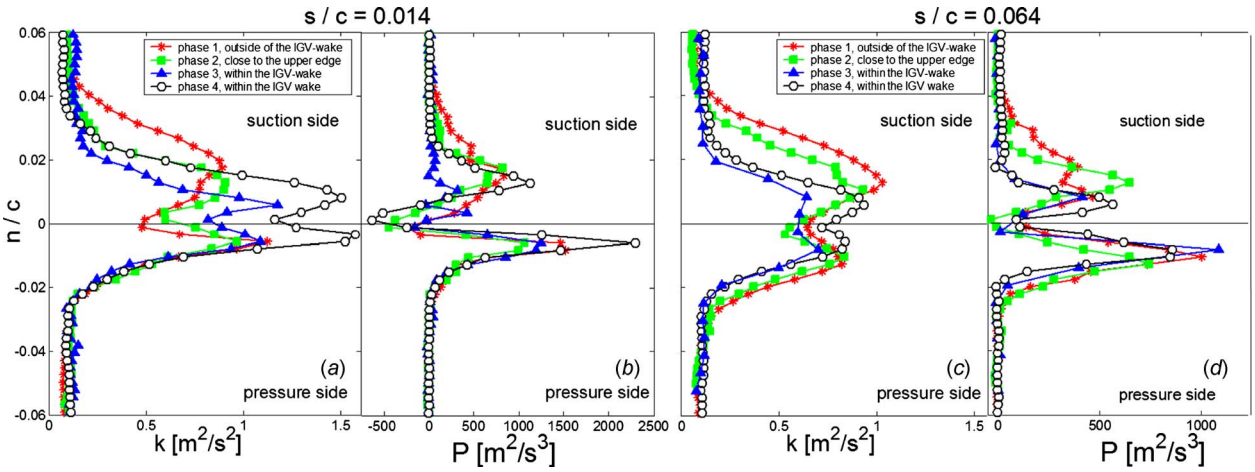

Fig. 15 Profiles of turbulent kinetic energy and its production rate at ((*a*)and (*b*)) *s*/*c*=0.014 and ((*c*) and (*d*)) *s*/*c*=0.064

as the wake clears the same regions. This phenomenon, associated with IGV-wake-induced changes of the free stream pressure gradients, has a direct impact on the flow and turbulence structure within the near rotor wake. Analysis performed in a newly defined wake-oriented coordinate system shows that thinning of the boundary/shear layer extends into the near-wake, making it narrower, and increasing magnitudes of shear velocity gradients and the shear production term. The latter is the dominant source of turbulence generation, and is constantly larger on the pressure side, where the shear layer is always thinner and the effects of IGV-wake-induced perturbations are small. As the IGV-wake clears the trailing edge, the boundary layer grows, the near-wake becomes thicker, and production in it decreases. Turbulent kinetic energy also increases during the process of thinning, with peak values moving closer to the wake centerline and upstream, toward the trailing edge, as the near-wake narrows down. Although peaks of TKE and production profiles occur in the same planes, asymmetries in production do not always correspond to similar asymmetries in TKE. Some of the differences are diminished by the effects of advection by the phase-averaged flow. Addressing in more detail these discrepancies requires (1) higher resolution data within the boundary layer, since the latter may feed different turbulence in the near-wake, and (2) data over many rotor phases, to follow the evolution of TKE accounting also for mean advection, transport terms, and dissipation rates.

Acknowledgment

This project is sponsored in part by the ONR under Grant No. N00014-03-1-0145, managed by Dr. Ki-Han Kim, and in part by the AFOSR under Grant No. FA9550-04-1-0019, managed by Lt. Col. Rhett Jefferies. We would like to thank Yury Ronzhes and Stephen King for their contribution to the construction and maintenance of the facility, and Dr. Yu-Tai Lee (NSWC/Carderock) for designing the blades.

Nomenclature

c = chord length (mm)
H = shape factor (δ^*/θ)
k = turbulent kinetic energy (m^2/s^2)
P = production rate of TKE (m^2/s^3)
R = radius of curvature (m)
s, n = streamwise (normal axis)
t = time (s)
u_i = instantaneous velocity (m/s)
U_{tip} = rotor blade tip speed (m/s)
$\bar{U}_\beta$ = velocity at a distance δ_β from the wake-center (m/s)
u_τ = friction velocity (m/s)
x,y,z = axial, lateral, and radial coordinates (mm)
α = flow angle ($\alpha=\tan^{-1}(\bar{U}_{y,r}/\bar{U}_x)$)
δ^* = boundary layer displacement thickness (mm)
δ_β = wake length scale (mm)
$\tilde{\varepsilon}$ = pseudodissipation (m^2/s^3)
θ = boundary layer momentum thickness (mm)
Π = transport term (m^2/s^3)
ν = kinematic viscosity (m^2/s)
ϕ = rotor phase angle (deg)
ω_z = vorticity component along z (1/s)
Ω = rotor angular velocity (rad/s)

Superscripts

w = wake
b = blade
$\bar{}$ = (overbar) phase-averaged properties
$'$ = fluctuating property
$[\,]$ = average of phase-averaged velocity over four rotor phases
$\sim$ = velocity perturbation ($\bar{U}_i-[\bar{U}_i]$)

Subscripts

p = potential
w = at the wall
r = relative frame of reference

References

[1] Patel, M. H., 1977, "On Turbulent Boundary Layers in Oscillatory Flows," Proc. R. Soc. London, Ser. A, **353**, pp. 121–144.
[2] Dibelius, G. H., and Ahlers, E., 1992, "Influence of Periodically Unsteady Wake Flow on the Flow Separation in Blade Channels," ASME J. Turbomach., **114**, pp. 108–113.
[3] Holland, R. M., and Evans, R. L., 1996, "The Effects of Periodic Wake Structures on Turbulent Boundary Layers," J. Fluids Struct., **10**(3), pp. 269–280.
[4] Gete, Z., and Evans, R. L., 2003, "An Experimental Investigation of Unsteady Turbulent-Wake/Boundary-Layer Interaction," J. Fluids Struct., **17**(1), pp. 43–55.
[5] Halstead, D. E., Wisler, D. C., Okishi, T. H., Walker, G. J., Hodson, H. P., and Shin, H. W., 1997, "Boundary Layer Development in Axial Compressors and Turbines: Part 1 of 4: Composite Picture," ASME J. Turbomach., **119**(1), pp. 114–127.
[6] Halstead, D. E., Wisler, D. C., Okishi, T. H., Walker, G. J., Hodson, H. P., and Shin, H. W., 1997, "Boundary Layer Development in Axial Compressors and Turbines: Part 2 of 4: Compressors," ASME J. Turbomach., **119**(3), pp. 426–444.
[7] Halstead, D. E., Wisler, D. C., Okishi, T. H., Walker, G. J., Hodson, H. P., and Shin, H. W., 1997, "Boundary Layer Development in Axial Compressors and Turbines: Part 3 of 4: LP Turbines," ASME J. Turbomach., **119**(2), pp. 225–237.
[8] Halstead, D. E., Wisler, D. C., Okishi, T. H., Walker, G. J., Hodson, H. P., and

Shin, H. W., 1997, "Boundary Layer Development in Axial Compressors and Turbines: Part 4 of 4: Computations and Analysis," ASME J. Turbomach., **119**(1), pp. 128–139.
[9] Mailach, R., and Vogeler, V., 2004, "Aerodynamic Blade Row Interactions in an Axial Compressor—Part I: Unsteady Boundary Layer Development," ASME J. Turbomach., **126**(1), pp. 35–44.
[10] Pfeil, H., and Herbst, R., 1979, "Transition Procedure of Instationary Boundary Layers," ASME Paper No. 79-GT-128.
[11] Mayle, R. E., and Dullenkopf, K., 1990, "A Theory for Wake-Induced Transition," ASME J. Turbomach., **112**(2), pp. 188–195.
[12] Hodson, H. P., Addison, J. S., and Shepherson, C. A., 1992, "Models for Unsteady Wake-Induced Transition in Axial Turbomachines," J. Phys. III, **2**, pp. 545–574.
[13] Cho, N.-H., Liu, X., Rodi, W., and Schonung, B., 1993, "Calculation of Wake-Induced Unsteady Flow in a Turbine Cascade," ASME J. Turbomach., **115**(4), pp. 675–686.
[14] Wu, X., and Durbin, P. A., 2000, "Boundary Layer Transition Induced by Periodic Wakes," ASME J. Turbomach., **122**(3), pp. 442–449.
[15] Schobeiri, M. T., Read, K., and Lewalle, J., 2003, "Effect of Unsteady Wake Passing Frequency on Boundary Layer Transition, Experimental Investigation, and Wavelet Analysis," ASME J. Fluids Eng., **125**(2), pp. 251–266.
[16] Liu, X., and Rodi, W., 1991, "Experiments on Transitional Boundary Layers With Wake-Induced Unsteadiness," J. Fluid Mech., **231**, pp. 229–256.
[17] Schobeiri, M. T., and Oztürk, B., 2003, "On the Physics of the Flow Separation Along a Low Pressure Turbine Blade Under Unsteady Flow Conditions," ASME Paper No. 2003-GT-38917.
[18] Schulte, V., and Hodson, H. P., 1994 "Wake-Separation Bubble Interaction in Low Pressure Turbines," AIAA, ASME, SAE, and ASEE 30th Joint Propulsion Conference and Exhibit, Indianapolis, IN, Jun. 27–29, AIAA Paper No. 94-2931.
[19] Stieger, R. D., and Hodson, H. P., 2003, "The Transition Mechanism of Highly-Loaded LP Turbine Blades," ASME Paper No. GT-2003-38304.
[20] Soranna, F., Chow, Y. C., Uzol, O., and Katz, J., 2006, "The Effect of Inlet Guide Vanes Wake Impingement on the Flow Structure and Turbulence Around a Rotor Blade," ASME J. Turbomach., **128**(1), pp. 82–95.
[21] Chow, Y.-C., Uzol, O., Katz, J., and Meneveau, C., 2005, "Decomposition of the Spatially Filtered and Ensemble Averaged Kinetic Energy, the Associated Fluxes and Scaling Trends in a Rotor Wake," Phys. Fluids, **17**(8), p. 085102.
[22] Soranna, F., Chow, Y. C., Uzol, O., and Katz, J., 2008, "Turbulence Within a Turbomachine Rotor Wake Subject to Nonuniform Contraction," AIAA J., **46**(11), pp. 2687–2702.
[23] Soranna, F., Chow, Y. C., Uzol, O., and Katz, J., 2006 "The Effect of IGV Wake Impingement on a Rotor Boundary Layer," *Proceedings of the 44th AIAA Aerospace Sciences Meeting and Exhibit*, Reno, NV, Jan. 8–12, AIAA Paper No. 2006-1305.
[24] Uzol, O., Chow, Y.-C., Katz, J., and Meneveau, C., 2002, "Unobstructed PIV Measurements Within an Axial Turbo-Pump Using Liquid and Blades With Matched Refractive Indices," Exp. Fluids, **33**(6), pp. 909–919.
[25] Golubev, V. V., and Atassi, H. M., 1996, "Sound Propagation in an Annular Duct With Mean Potential Swirling Flow," J. Sound Vib., **198**(5), pp. 601–616.
[26] Roth, G. I., Mascenik, D. T., and Katz, J., 1999, "Measurements of the Flow Structure and Turbulence Within a Ship Bow Wave," Phys. Fluids, **11**(11), pp. 3512–3523.
[27] Roth, G. I., and Katz, J., 2001, "Five Techniques for Increasing the Speed and Accuracy of PIV Interrogation," Meas. Sci. Technol., **12**, pp. 238–245.
[28] Hodson, H. P., and Dawes, W. N., 1998, "On the Interpretation of Measured Profile Losses in Unsteady Wake-Turbine Blade Interaction Studies," ASME J. Turbomach., **120**(2), pp. 276–284.
[29] Meyer, R. N., 1958, "The Effect of Wakes on the Transient Pressure and Velocity Distribution in Turbomachines," ASME J. Basic Eng., **80**, pp. 1544–1552.
[30] Wheeler, A., Miller, R., and Hodson, H., 2007, "The Effect of Wake Induced Structures on Compressor Boundary-Layers," ASME J. Turbomach., **129**, pp. 705–712.
[31] So, R. M. C., and Mellor, G. L., 1973, "Experiment on Convex Curvature Effects in Turbulent Boundary Layers," J. Fluid Mech., **60**, pp. 43–62.
[32] Hah, C., and Lakshminarayana, B., 1982, "Measurements and Prediction of Mean Velocity and Turbulence Structure in the Near Wake of an Airfoil," J. Fluid Mech., **115**, pp. 251–282.
[33] Pope, S. B., 2000, *Turbulent Flows*, Cambridge University, Cambridge, UK.